International Forum on Aeroelasticity and Structural Dynamics
IFASD 2017
25–28 June 2017, Como, Italy

ENABLING PRACTICAL WING DESIGN VIA HIGH-FIDELITY MULTIDISCIPLINARY OPTIMIZATION

Joaquim R. R. A. Martins[1] **and Timothy R. Brooks**[1]

[1]Department of Aerospace Engineering
University of Michigan, Ann Arbor MI 48103, USA

Keywords: aeroelasticity, aerostructural optimization, multidisciplinary design optimization, aircraft design

Abstract: Wing shape is a crucial aircraft component that has a large impact performance. Wing design optimization has been an active area of research for several decades, but achieving practical designs has been a challenge. One of the main challenges is the wing flexibility, which requires the consideration of both aerodynamics and structures. To address this, we have developed the capability to perform simultaneous optimization of the outer mold line of a wing and its structural sizing. The solution of such design optimization problems is made possible by MACH, a framework for high-fidelity aerostructural optimization that uses state-of-the-art numerical methods. MACH combines a three-dimensional CFD solver, a finite-element structural model of the wingbox, a geometry modeler, and a gradient-based optimizer. It computes the flying shape of a wing and is able to optimize aircraft configurations with respect to hundreds of aerodynamic shape and internal structural sizes. The theoretical developments include coupled-adjoint sensitivity analysis, and an automatic differentiation adjoint approach. The algorithms resulting from these developments are all implemented to take advantage of massively parallel computers. To benchmark the developed approaches, we created a high-fidelity aeroelastic model based on NASA's Common Research Model. In addition, we created a high aspect ratio wing version of this model to explore the use of new aircraft technologies. Applications to the optimization of aircraft configurations demonstrate the effectiveness of these approaches in designing aircraft wings for maximum performance.

1 INTRODUCTION

Wing design was one of the of the first applications of multidisciplinary design optimization (MDO) because it is an application where aerodynamics, structures, and controls are strongly coupled disciplines, requiring both the consideration of the coupled (multidisciplinary) analysis and design trade-offs [1–6]. MDO has also been used to perform aircraft sizing [7, 8] and has been applied to a wide range of other applications [9]. When optimizing both aerodynamics and structures, we need to consider the effect of the aerodynamic shape variables and structural sizing variables on the weight, which also affects the fuel burn. Numerical optimization is a powerful tool that can perform these complex trade-offs automatically.

In this paper, we present an overview of a decade of efforts in our research group towards enabling practical wing design with high-fidelity MDO. We start by describing the key numerical techniques and software that make it possible to solve design optimization that would previously be considered intractable due to the high cost of the simulations, the large number of

design variables, the large number of constraints, and the multiple flight conditions. The techniques leverage state-of-the-art CFD and structural solvers with adjoint methods for computing derivatives, together with a gradient-based optimizer. We then present several applications of these techniques to wing design. The first application is a new benchmark for aeroelastic wing design studies based on NASA's Common Research Model aircraft configuration, including both a conventional aspect ratio wing, and a higher aspect ratio wing meant to represent a next generation wing. We present other applications also related to NASA's efforts to develop high aspect ratio wings for the next generation of airliners.

2 NUMERICAL TECHNIQUES AND SOFTWARE

2.1 Numerical optimization

Numerical optimization algorithms automatically close the design cycle by iteratively finding the design variables that maximize the performance subject to design constraints. There are two main classes of optimization algorithms: gradient-based and gradient-free algorithms. Gradient-free algorithms require only the values of the objective and constraint functions, while gradient-based algorithms also require the gradients of these functions with respect to the design variables. Gradient-based methods utilize the gradient information to find the most promising directions in the design variable space, and converge to the optimum more quickly. The optimization algorithm we use for all the results presented herein is SNOPT (sparse nonlinear optimizer) [10] through the Python interface pyOpt [11].

Fig. 1 illustrates how the various optimization algorithms scale with the number of design variables. The number of function evaluations for the gradient-free optimizers (ALPSO, NSGA2) scales exponentially, and it becomes intractable to perform optimization with respect to $\mathcal{O}(10^2)$ design variables. On the other hand, the gradient-based algorithms (SNOPT, SLSQP) scale much better, exhibiting linear convergence or better depending on the method used to compute the gradients. Computing the derivatives analytically makes a big difference, and thus, computing derivatives accurately and efficiently is essential for efficient gradient-based optimization.

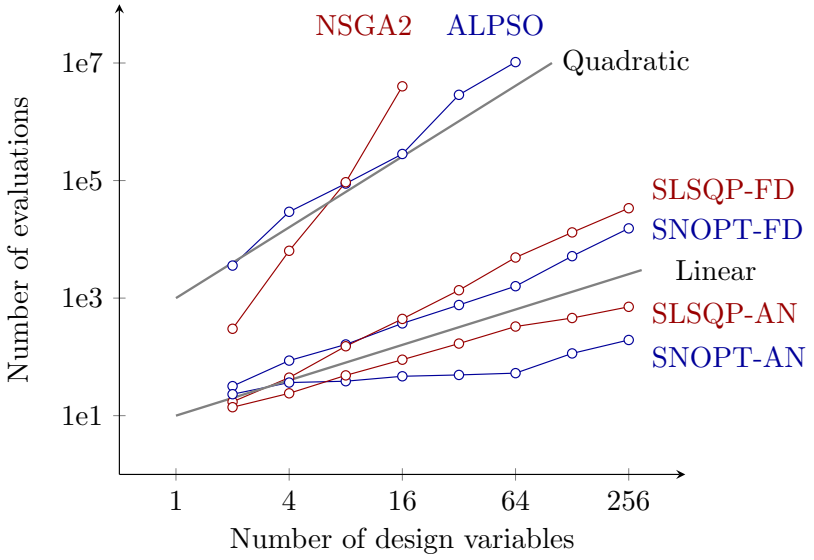

Figure 1: Computational cost required to minimize a constrained multidimensional Rosenbrock function with respect to the number of design variables.

2.2 Derivative computation methods

To solve an optimization problem, a gradient-based algorithm requires the derivatives of the objective function with respect to each design variable, and the derivatives of all the constraints with respect to the design variables [12].

Finite-difference approximations are widely used to compute derivatives due to their simplicity and the fact that they can be implemented even when a the function evaluation is provided as black box. However, the cost of computing a gradient using finite differences is proportional to the number of design variables. Another disadvantage of finite-differences is the *step-size dilemma*: we want to reduce the truncation error by reducing the step size, but as this step size is reduced, errors due to subtractive cancellation become dominant and eventually this results in inaccurate estimates.

The *complex-step derivative approximation* does away with the step-size dilemma by providing a formula that does not involve subtraction. This estimate is very accurate, insensitive to step size, and easy to implement [13, 14]. However, the cost of computing a gradient is still proportional to the number of design variables. The complex-step method has been shown to be generally applicable to any computer program [14].

Automatic differentiation (AD) is based on the systematic symbolic differentiation of each line of a computer program, and the accumulation of total derivatives using the chain rule. The method relies on tools that automatically produce a program that computes user-specified derivatives based on the original program [15]. There are two modes for AD: the forward mode and the reverse mode. The forward mode propagates the chain rule forward, while the reverse mode does it backward after executing the original code. The reverse mode, while more complex, has the advantage that the cost of computing a gradient is independent of the number of design variables. There are automatic differentiation tools available for a variety of programming languages including C/C++, and Fortran [16–20].

Analytic methods are based on the linearization of the numerical model equations. Like AD, the numerical precision of analytic methods is the same as that of the original algorithm. In addition, analytic methods are usually more efficient than AD for a given problem. However, analytic methods are much more involved than the other methods, since they require detailed knowledge of the computational model and a long implementation time. Analytic methods are applicable when we have a quantity of interest f that depends implicitly on the independent variables of interest x as follows

$$f = F(x, y(x)). \tag{1}$$

The implicit relationship between the state variables y and the independent variables is defined by the solution of a set of governing equations that can be written as residuals,

$$r = R(x, y(x)) = 0. \tag{2}$$

As a first step toward obtaining the derivatives that we want to compute, we use the chain rule to write the total derivative of f as

$$\frac{\mathrm{d}f}{\mathrm{d}x} = \frac{\partial F}{\partial x} + \frac{\partial F}{\partial y}\frac{\mathrm{d}y}{\mathrm{d}x}, \tag{3}$$

In this context, the partial derivatives represent the variation of $f = F(x)$ with respect to changes in x for a fixed y, while the total derivative $\mathrm{d}f/\,\mathrm{d}x$ takes into account the change in y

that is required to keep the residual equations (2) equal to zero. Since the governing equations must always be satisfied, the total derivative of the residuals (2) with respect to the design variables must also be zero. Thus, using the chain rule we obtain

$$\frac{\mathrm{d}r}{\mathrm{d}x} = \frac{\partial R}{\partial x} + \frac{\partial R}{\partial y}\frac{\mathrm{d}y}{\mathrm{d}x} = 0. \tag{4}$$

The computation of the total derivative matrix $\mathrm{d}y/\,\mathrm{d}x$ has a much higher computational cost than any of the partial derivatives, since it requires the solution of the residual equations (2). Rearranging the linearized residual equations (4) we can compute the total derivative matrix $\mathrm{d}y/\,\mathrm{d}x$ by solving the linear system,

$$\frac{\partial R}{\partial y}\frac{\mathrm{d}y}{\mathrm{d}x} = -\frac{\partial R}{\partial x}. \tag{5}$$

Substituting this result into the total derivative equation (3), we obtain

$$\frac{\mathrm{d}f}{\mathrm{d}x} = \frac{\partial F}{\partial x} - \underbrace{\frac{\partial F}{\partial y}\overbrace{\left[\frac{\partial R}{\partial y}\right]^{-1}}^{-\frac{\mathrm{d}y}{\mathrm{d}x}}}_{\psi}\frac{\partial R}{\partial x}. \tag{6}$$

The inverse of the square Jacobian matrix $\partial R/\partial y$ is not necessarily calculated explicitly. We use the inverse to denote that this matrix needs to be solved as a linear system with some right-hand-side vector. Eq. (6) shows that there are two ways of obtaining the total derivative matrix $\mathrm{d}y/\,\mathrm{d}x$, depending on which right-hand side is chosen for the solution of the linear system.

The *direct method* solves the linear system with $-\partial R/\partial x$ as the right-hand side vector, which results in the linear system (5). This linear system needs to be solved for each design variable to get the full Jacobian matrix $\mathrm{d}y/\,\mathrm{d}x$. Then, we can use $\mathrm{d}y/\,\mathrm{d}x$ in Eq. (3) to obtain the derivatives of interest, $\mathrm{d}f/\,\mathrm{d}x$. As in the case of finite differences, the cost of computing derivatives with the direct method is proportional to the number of design variables.

The *adjoint method* is an alternative whose cost does not depend on the number of design variables. The adjoint equation is encapsulated in the total derivative equation (6), where we observe that there is an alternative option for computing the total derivatives: the linear system involving the large square Jacobian matrix $\partial R/\partial y$ can be solved with $\partial f/\partial y$ as the right-hand side. This results in the *adjoint equations*,

$$\left[\frac{\partial R}{\partial y}\right]^T \psi = -\left[\frac{\partial F}{\partial y}\right]^T, \tag{7}$$

which is a linear systems where ψ is the *adjoint vector*. The adjoint vector can then be substituted into Eq. (6) to find the total derivative,

$$\frac{\mathrm{d}f}{\mathrm{d}x} = \frac{\partial F}{\partial x} + \psi^T\frac{\partial R}{\partial x}. \tag{8}$$

The partial derivatives shown in these equations need to be computed using some other method. They can be differentiated symbolically or computed by finite differences, the complex-step method, or even AD. The use of AD to automatically produce the code that computes these partials derivatives has shown to be particularly effective in the development of analytic methods for PDE solvers [21–23].

2.3 Aerostructural optimization

The aerostructural shape optimization procedure used in the MDO for aircraft with high-fidelity (MACH) framework is illustrated in Fig. 2. The optimization loop relies on a gradient-based optimization algorithm (SNOPT) to decide on the new set of design variables x at each iteration. For each new set of design variables, we must generate a new geometry and corresponding CFD mesh and structural model so that the flow solver can compute the drag, lift, and moment coefficients, as well as the wing flying shape. A coupled adjoint solver then computes the derivatives required by the optimization algorithm to perform the next design optimization iteration. MACH has been successfully used to perform several studies for both aerodynamic [24–29] and aerostructural design studies [6, 30–34].

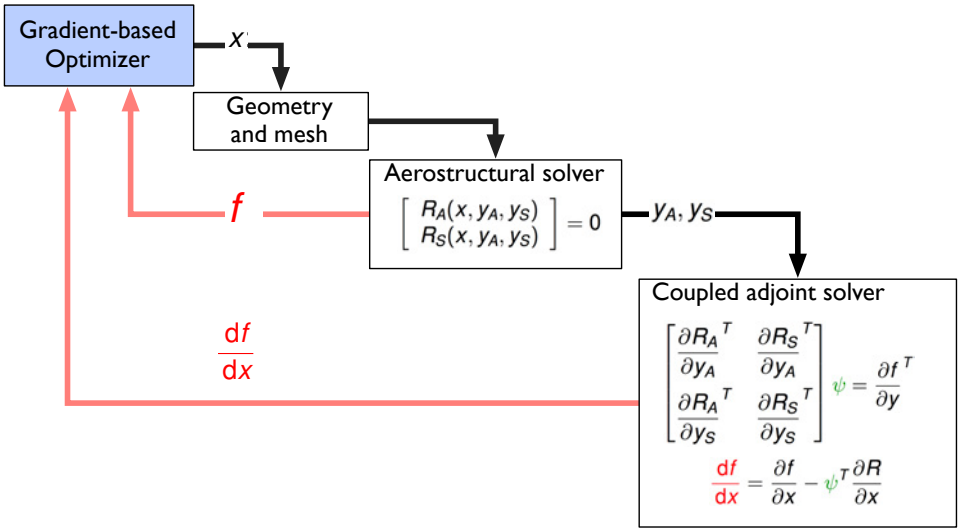

Figure 2: Aerostructural design optimization cycle.

2.3.1 CFD solver

The CFD solver used in the work herein is ADflow, which is a finite-volume, cell-centered multiblock solver for the compressible Euler, laminar Navier–Stokes, and RANS equations (steady, unsteady, and time-periodic modes) [35]. Recently, overset mesh capability was added to ADflow, facilitating its application to complex aircraft geometries. ADflow also includes a matrix-free adjoint method implementation that relies on AD to compute the partial derivative terms in Eqs. (7) and (8)

2.3.2 Geometry and mesh movement

For manipulating the geometry, we use a free-form deformation (FFD) volume approach [36] that we implemented [37] and have been using extensively for aerodynamic [24–29] and aerostructural optimization studies [6, 30, 34, 38]. The FFD approach can be visualized as embedding the spatial coordinates defining a geometry inside a flexible volume. The parametric locations corresponding to the baseline geometry are found using a Newton search algorithm. Once the baseline geometry has been embedded, perturbations made to the FFD volume propagate within the embedded geometry via the evaluation of the nodes at their parametric locations.

The FFD approach used to parametrize the geometry applies deformations only to the surface mesh—the part of the volume mesh that lies on the physical surface. A mesh movement pro-

cedure is then required to propagate surface perturbations to the remainder of the CFD volume mesh. The mesh movement algorithm used in this work is an efficient analytic inverse distance method [39].

2.3.3 Structural solver

The structural solver we developed is the Toolkit for the Analysis of Composite Structures (TACS) [40]. TACS includes an adjoint solver that is able to handle the structural design variables, which in our case are the thicknesses of the structural members. Parallelism is achieved within TACS by using an element-based partitioning of the finite-element mesh. This partitioning is used to parallelize the factorization of the stiffness matrix, the computation and assembly of the stiffness matrix and structural residuals, and the computation of the functions of interest and their derivatives.

2.3.4 Aerostructural solver

Coupling aerodynamic and structural numerical models to compute the static aeroelastic shape of lifting surfaces is essential when designing lifting surfaces that are flexible. Even small changes in shape can have a large effect on the aerodynamic performance, and multiple flow conditions result in multiple shapes. This is particularly important for swept wings, where bend-twist coupling can result in large changes in the twist distribution.

The load and displacement transfer scheme we use follows the work of Brown [41]. In this approach, rigid links are used to extrapolate the displacements from the structural surface to the CFD surface, as shown in Fig. 3. These rigid links are constructed between the aerodynamic surface mesh points and the points on the structural model lying closest to this set of points. The consistent force vector is determined by employing the method of virtual work, ensuring that the force transfer is conservative. The integration of the forces is performed on the aerodynamic mesh and is transmitted back through the rigid links to the structure. More details on these transfers can be found in previous work [38, 41, 42]

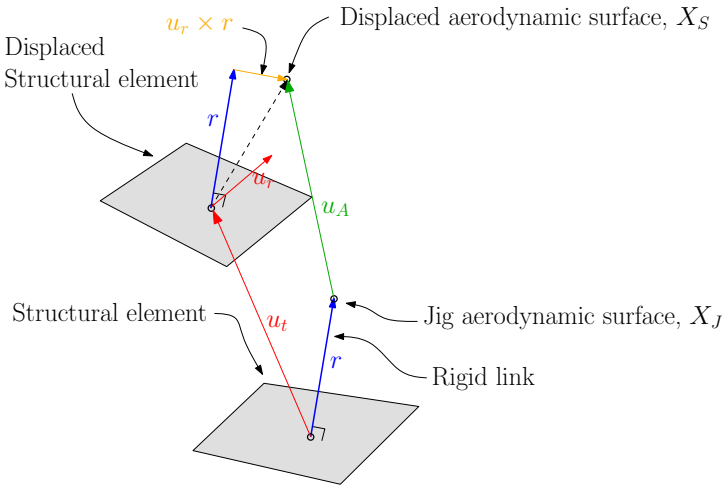

Figure 3: Load-displacement transfer operation

We formulate the aerostructural analysis problem using a two-field formulation. Using this formulation, we can write the governing equations of both disciplines as a function of the fluid states, w, structural states, u, and design variables x. Combining the residual equations from the

aerodynamic and structural disciplines, we write the combined residual of the multidisciplinary system as

$$\mathcal{R} = \begin{bmatrix} \mathcal{A}(w, u; x) \\ \mathcal{S}(u, w; x) \end{bmatrix} = 0. \tag{9}$$

The aerostructural analysis consists in finding a solution, (w, u), that satisfies these coupled residual equations.

The traditional process for solving the coupled aerostructural equations (9) is to use a nonlinear block Gauss–Seidel (NLBGS) method [43, 44]. In this approach, the aerodynamic analysis is first partially converged and the aerodynamic forces are evaluated. The forces are then transferred to the structural analysis and the corresponding displacements are computed. Finally, the displacements are transferred back to the aerodynamic analysis, the mesh is deformed, a new CFD solution is found, and this iterative loop continues until the coupled convergence criterion is met. Aitken acceleration [45] is used to dynamically choose the under-relaxation factor to accelerate convergence. We also implemented a fully coupled Newton–Krylov (CNK) method for solving the aerostructural equations in a monolithic fashion. We use an inexact Newton–Krylov approach to solve the coupled equations (9).

2.3.5 Coupled adjoint derivatives

One of the critical components of the aerostructural framework is an efficient method for the computing coupled derivatives. Using the coupled adjoint approach [43], we write the adjoint equations for the aerostructural system. The total derivative of the function of interest, f, is

$$\frac{\mathrm{d}f}{\mathrm{d}x} = \frac{\partial f}{\partial x} + \begin{bmatrix} \dfrac{\partial f}{\partial w} & \dfrac{\partial f}{\partial u} \end{bmatrix} \begin{bmatrix} \dfrac{\mathrm{d}w}{\mathrm{d}x} \\ \dfrac{\mathrm{d}u}{\mathrm{d}x} \end{bmatrix}. \tag{10}$$

We write the total derivative of the residuals as

$$\begin{bmatrix} \dfrac{\mathrm{d}\mathcal{A}}{\mathrm{d}x} \\ \dfrac{\mathrm{d}\mathcal{S}}{\mathrm{d}x} \end{bmatrix} = \begin{bmatrix} \dfrac{\partial \mathcal{A}}{\partial x} \\ \dfrac{\partial \mathcal{S}}{\partial x} \end{bmatrix} + \begin{bmatrix} \dfrac{\partial \mathcal{A}}{\partial w} & \dfrac{\partial \mathcal{A}}{\partial u} \\ \dfrac{\partial \mathcal{S}}{\partial w} & \dfrac{\partial \mathcal{S}}{\partial u} \end{bmatrix} \begin{bmatrix} \dfrac{\mathrm{d}w}{\mathrm{d}x} \\ \dfrac{\mathrm{d}u}{\mathrm{d}x} \end{bmatrix} = 0. \tag{11}$$

Substituting the solution of Eq. (11) into Eq. (10) to eliminate the total derivatives we obtain

$$\frac{\mathrm{d}f}{\mathrm{d}x} = \frac{\partial f}{\partial x} - \underbrace{\begin{bmatrix} \dfrac{\partial f}{\partial w} & \dfrac{\partial f}{\partial u} \end{bmatrix} \begin{bmatrix} \dfrac{\partial \mathcal{A}}{\partial w} & \dfrac{\partial \mathcal{A}}{\partial u} \\ \dfrac{\partial \mathcal{S}}{\partial w} & \dfrac{\partial \mathcal{S}}{\partial u} \end{bmatrix}^{-1}}_{\Psi^T} \begin{bmatrix} \dfrac{\partial \mathcal{A}}{\partial x} \\ \dfrac{\partial \mathcal{S}}{\partial x} \end{bmatrix}. \tag{12}$$

This yields the coupled adjoint equations,

$$\begin{bmatrix} \dfrac{\partial \mathcal{A}}{\partial w} & \dfrac{\partial \mathcal{A}}{\partial u} \\ \dfrac{\partial \mathcal{S}}{\partial w} & \dfrac{\partial \mathcal{S}}{\partial u} \end{bmatrix}^T \begin{bmatrix} \psi \\ \phi \end{bmatrix} = \begin{bmatrix} \dfrac{\partial f}{\partial w} & \dfrac{\partial f}{\partial u} \end{bmatrix}^T. \tag{13}$$

After the solution for the coupled adjoint equations (13) is obtained, the following equation can be used to compute the total derivative:

$$\frac{\mathrm{d}f}{\mathrm{d}x} = \frac{\partial f}{\partial x} - \psi^T \left(\frac{\partial \mathcal{A}}{\partial x} \right) - \phi^T \left(\frac{\partial \mathcal{S}}{\partial x} \right). \tag{14}$$

Implementing the coupled adjoint, including all the required partial-derivative terms, is a challenging endeavor. Furthermore, ensuring that the partial-derivative computations and solution methods are efficient and exhibit good parallel scalability is even more difficult. More details on what these partial derivatives mean and how they are computed are provided in previous work [38, 42].

As with the aerostructural system of equations, we consider two approaches to solve the coupled adjoint system (13): a segregated approach and a monolithic approach. The segregated approach is the lagged coupled adjoint approach [46], which corresponds to a linear block Gauss–Seidel algorithm. We also implemented a monolithic approach, which uses a Krylov method applied directly to the coupled linear system.

3 A BENCHMARK FOR HIGH-FIDELITY WING DESIGN

The NASA Common Research Model (CRM) was developed to be representative of a long-range twin-aisle transport aircraft and has been used primarily as a CFD benchmark for drag prediction [47], and the Aerodynamic Design Optimization Discussion Group (ADODG) benchmarks [28, 48–53]. Since we want a benchmark model for aeroelastic studies, and CRM geometry only provides the 1 g wing shape, we developed a structural wing box model and a jig wing shape, which we call the undeflected CRM (uCRM) [34], shown in Figure 4.

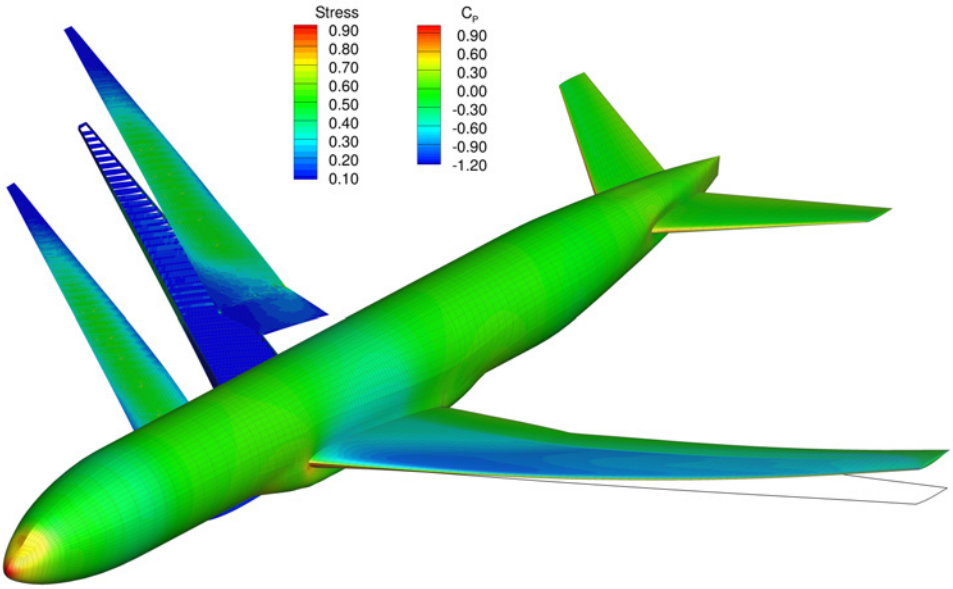

Figure 4: uCRM aerostructural model with wingbox structural model (left) aerodynamic model (right); the black line denotes the wing jig shape.

Because of the growing interest in aerostructural analysis and optimization on the CRM model and future high aspect ratio wing designs, we would like to standardize two aerostructural benchmark geometries: an aspect ratio 9 wing based on the CRM, the *uCRM-9*, and a higher aspect ratio (13.5), variant, the *uCRM-13.5*. Since aerostructural analysis will be performed using these models, the 1 g "built-in" deflections become problematic and we must instead define the jig (undeflected) shape. The goal is that these models provide a useful benchmark for aeroelastic studies. To this end, all files associated with these designs—both geometry and mesh files—are publicly available.

There have already been a number of efforts utilizing higher fidelity static aerostructural optimization, featuring a RANS-based CFD solver coupled with a computational structural mechanics (CSM) solver using the aspect ratio (AR) 9 model, the uCRM-9 [30, 34, 54]. Due to a continual push for increased aircraft efficiency and reduction in fuel burn, there is a growing interest in enabling high aspect ratio wings through the use of future technologies such as tow-steered composites [31, 55], morphing trailing edge wings [32], and additive manufactured wingbox topologies [56]. Each of these studies was conducted using the uCRM-13.5 configuration as the baseline.

One of the aspects that has previously been neglected in aerostructural design optimization is buffet mitigation. Buffet occurs when a shock wave oscillates in position due to an interaction with the separated boundary layer. These oscillations grow and eventually become unstable. This unsteady phenomenon leads to undesirable effects, such as flow separation and intense structural vibrations. To address this issue, we use a separation-based buffet onset prediction metric based on steady CFD that has shown to be valid for the CRM [57].

3.1 uCRM-9: An undeflected version of the Common Research Model

For both the uCRM-9 and the uCRM-13.5, we only model the structure of the wingbox. We had to design a jig shape and structural model for the wing, since no such model currently exists. We designed uCRM-9 model with a jig shape and structure that deforms into the shape of the original outer mold line (OML) of the CRM model at a nominal cruise condition ($M = 0.85$, $C_L = 0.5$ at 37 000 ft) [58]. This structural design was done through an inverse design procedure. First, we defined a wingbox layout based on a similar aircraft, and sized the structure using representative aerodynamic loads. We then applied an inverse design procedure that iteratively removed the deflection from the OML and wingbox geometry, while updating the structural sizing to ensure that the aeroelastically deflected shape matched the nominal deflection profile of the CRM. This is identical to the design procedure we used previously [34].

As the first step of the uCRM-9 design process, we start by defining a realistic wingbox layout. Since there is no publicly available data on wingboxes for modern transport aircraft, we based our layout on cutaway views of the Boeing 777-200ER aircraft. Figure 5 shows the planform view of the 777-200ER extracted from the aircraft planning document [59] with a best-guess superimposed wingbox locations (left), as well as the planform of the CRM and our wingbox layout (right). Using digital versions of the Boeing 777 drawing, we estimate the extent of the wingbox at the root and tip. This information was sufficient to define the wingbox structure planform for the CRM geometry. We generate the wingbox for the CRM using the same proportions (front and rear spar location, rib spacing, etc.) and structural layout of the Boeing 777 wingbox. Due to differences in sweep and span, we could not implement the approximated wingbox layout for the Boeing 777 directly in the CRM planform.

Once we defined the planform of the wingbox, we used an in-house tool to generate the geometry of the wingbox and its components conforming with the wing OML. We use a fixed aerodynamic load distribution to recover the undeflected shape of the wing. We convert the converged aerodynamic pressure and skin friction forces to tractions, which are used to size the wingbox, and later used for the inverse design procedures. The wingbox elements are sized through numerical optimization for the given fixed aerodynamic loads. All components in the wingbox structure are modeled using aluminum 7000 series alloy.

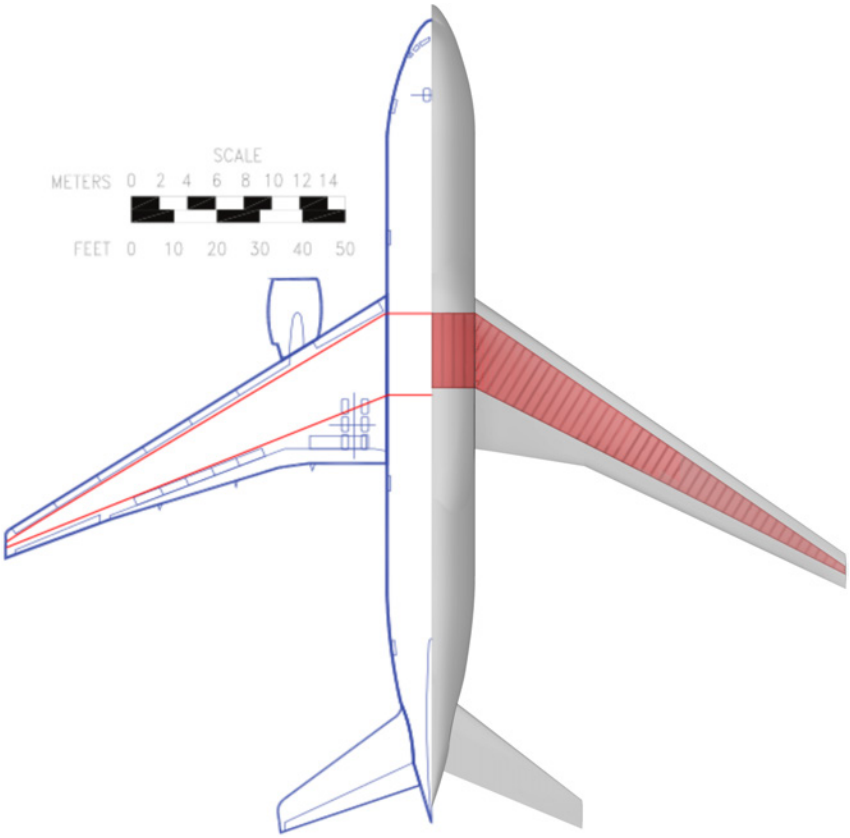

Figure 5: Boeing 777 (left) and uCRM-9 (right). The CRM has a slightly lower wing area and span, and more sweep than the Boeing 777.

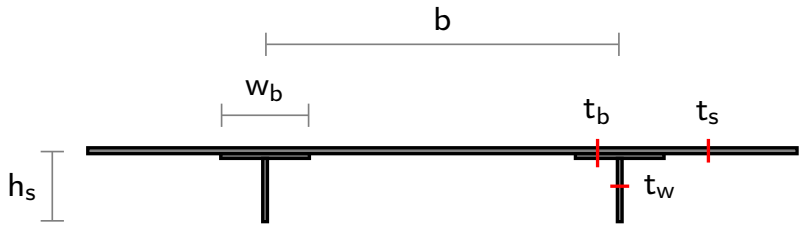

Figure 6: Panel-stiffener parametrization assumed by the smeared stiffness approach [60].

Like all modern transport aircraft, our wingbox uses blade stiffened panels for the main components. The stiffeners are not included explicitly in the finite element model of the wingbox. Instead, we model the effect of their stiffness by homogenizing (or smearing) them into the wingbox panels stiffness. Kennedy et al. [60] describe the smeared stiffness approach in more detail. Fig. 6 shows the assumed general cross-section of a wingbox panel under the smeared stiffness approach, where we link the blade and flange thicknesses ($t_w = t_b$) and the blade height to the flange width ($w_b = h_s$). Using this approach, we can perform panel-level buckling analysis while considering multiple buckling modes. These buckling modes include: intra-stiffener skin buckling, stiffener buckling, and coupled stiffener-skin buckling modes. All three buckling modes are aggregated into a single scalar value using a Kreisselmeier–Steinhauser (KS) function [61, 62], which gives a conservative approximation to the most violated case.

The structural sizing of the wingbox was produced through a structural optimization. The optimization consisted in minimizing the mass while enforcing failure and buckling constraints at a

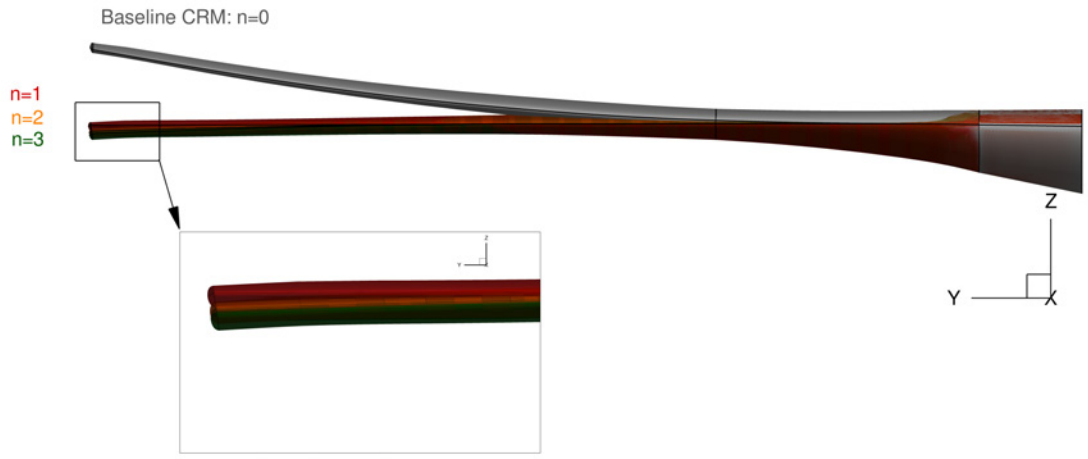

Figure 7: Inverse design iteration history for uCRM-9 wing jig.

2.5 g maneuver load. The skin, ribs, and spar panels were constrained not to fail or buckle with a safety factor of 1.5. The structural analysis included inertial load relief from the structure, engine, and fuel. The design variables are stiffener pitch (spacing), stiffener height, stiffener thickness, and panel thickness. The stiffener pitch for the upper and lower skins are equal everywhere. The remaining structural variables are free to change (within their bounds) from one panel to the next. The initial optimized wingbox provides an initial guess for the structure of the wing jig shape. However, because this first guess is based on the CRM OML it also features the "built-in" 1 g deflection in its geometry. We remove this deflection in the subsequent inverse design procedure, so that the CRM wing geometry can be recovered from the jig through structural deflection of the wingbox.

Given the 1 g OML of the original CRM, the wingbox structural layout and sizing, as well as the aerodynamic loads, we now determine the jig shapes for the OML and wingbox. This is accomplished by solving a least square optimization problem where we minimize the difference between the CRM OML points, X_T, and points on the deflected jig shape under the nominal 1 g loads, X_{deflect}. The deflected points are found by taking the jig points and adding the structural deflections from the applied aerodynamic loads ($X_{\text{deflect}} = X_{\text{jig}} + u$). The optimizer change only the geometry of the wing jig through the FFD x, y, and z coordinates to match the two sets of points, such that the initial deflection of the CRM wing is achieved through structural deflection only. This inverse design procedure needs to be applied multiple times since as the geometry of the structure changes, so too do the structural deflections, u. Once the FFD shape variables are found, we apply them to the initial CRM geometry and wingbox to remove the deflection and achieve a new approximate jig geometry. The new structural geometry is then structurally resized using another structural optimization and the procedure is repeated until convergence. In our case, three inverse design cycles were required before a converged jig solution was achieved. Fig. 7 shows the sequence of inverse design results leading to the finalized wing jig. To verify the resulting jig shapes and wingbox sizing, we performed an aerostructural analysis of the uCRM-9 and compare it to the aerodynamic analysis of the CRM [34].

3.2 uCRM-13.5: A benchmark for high aspect ratio wing design

The uCRM-13.5 model is the result of a full aerostructural design optimization where the OML is optimized in addition to the structural sizing. This is in contrast with the uCRM-9 model, where the CRM OML is preserved, and only a structural sizing optimization is performed. The

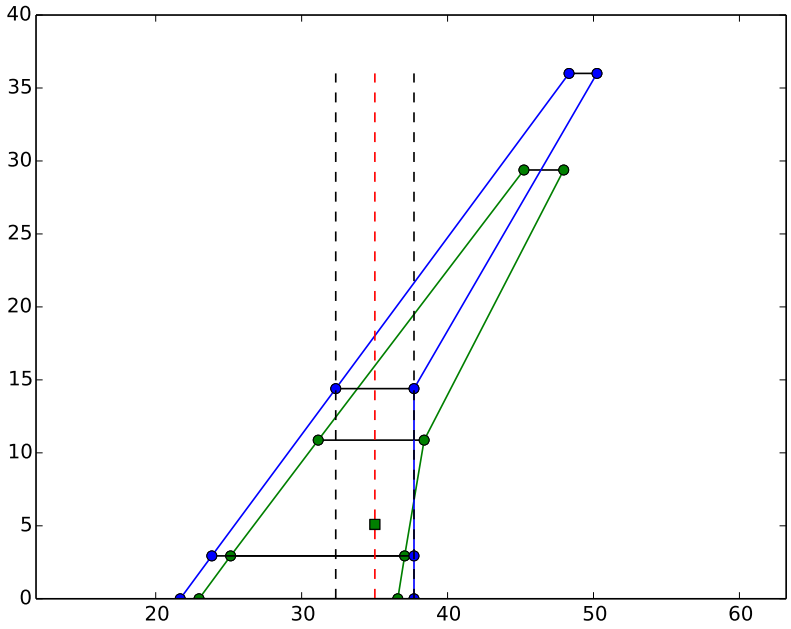

Figure 8: uCRM-13.5 wing planform (blue) and CRM-9 planform (green). The dotted lines show the 0, 50% and 100% MAC locations for the uCRM-13.5. The green dot at 50%MAC shows the main gear post location.

uCRM-13.5 wing maintains overall compatibility with the remainder of the CRM aircraft. In this way, the resulting aircraft design may be considered to be a higher span derivative of the CRM. The goal of his model is to develop a modification of the well-tested CRM configuration compatible with that configuration. The extension of the uCRM-9 to obtain the required 13.5 aspect ratio is complicated by the fact that we want to preserve the same wing loading and landing gear location to avoid a cascade of changes that would affect the aircraft sizing. The uCRM-13.5 wing planform was designed by taking the uCRM-9 planform and extending the wing span until an aspect ratio of 13.5 was achieved. The wing area was kept constant, to ensure that the wing loading remained unchanged. The uCRM-13.5 wing is shifted forward to preserve similar longitudinal stability characteristics. A rendering of the uCRM-13.5 planform is shown in Fig. 9.

The structural wingbox planform is shown in Fig. 9. We designed the uCRM-13.5 wingbox to have the same topology as the uCRM-9, with the exception of the number of ribs. The absolute spacing was kept the same, and hence the uCRM-13.5 has 9 additional ribs for a total of 54. The trailing edge spar also features a more distinctive kink at the Yehudi break. This was done to move the spar forward in this region and ensure that the spar depth did not become so small as to become a manufacturing concern. The engine is also assumed to be mounted in the same absolute spanwise position.

Like the uCRM-9 design, we based the uCRM-13.5 on a traditional aluminum wingbox structure. A 13.5 AR wing is pushing the limits of what is currently possible with conventional aluminum wing design. As a result, if we perform an aerostructural analysis of this model while keeping a similar cross-sectional, twist, and structural sizing distribution as the uCRM-9, the design performs poorly due to the additional structural deformation caused by the increased wing flexibility. For this reason, unlike for uCRM-9, we perform an aerostructural design optimization that takes these effects into account. Buffet onset constraints were also included for

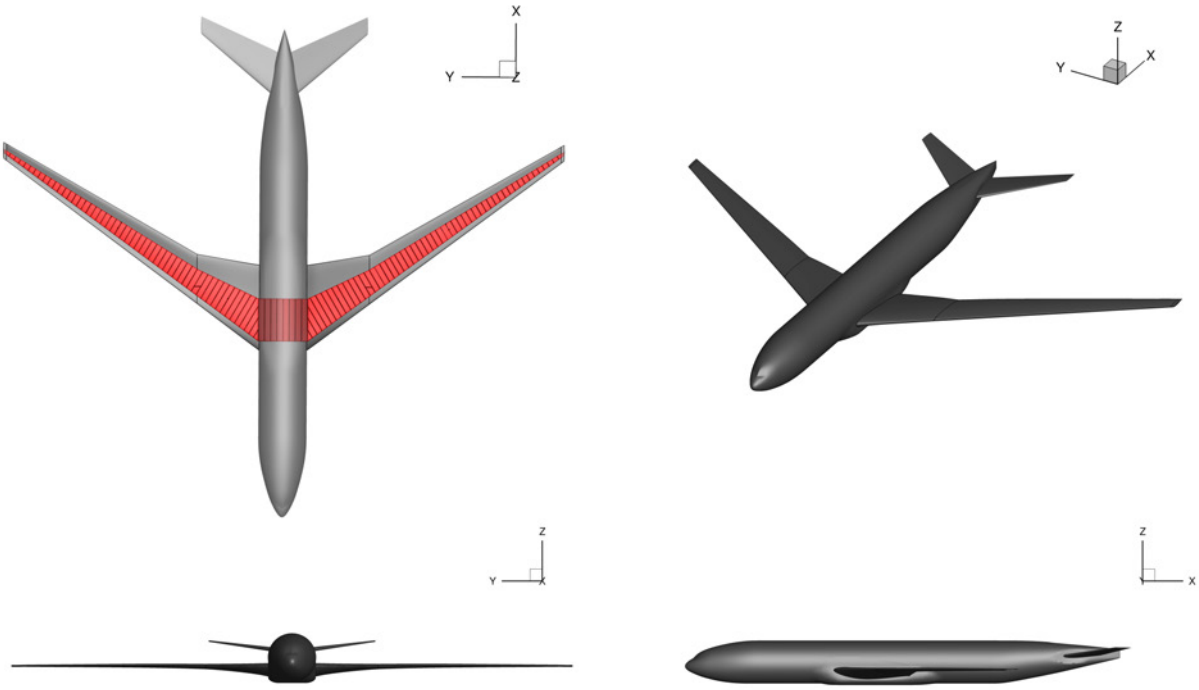

Figure 9: Three view of the uCRM-13.5 wing planform and structural geometry.

the design optimization to obtain a wing that can be used for a transonic transport.

The flight conditions considered consist of a five point cruise stencil: two buffet constraint conditions, and three maneuver conditions. The initial optimization flight conditions are detailed in Table 1, where MTOW is the maximum takeoff weight of the aircraft. The five cruise design conditions form a cross in Mach-C_L space. This is done to ensure that the fuel burn of the design is robust for varying aircraft weights and flight conditions. The center of the cruise stencil, condition 1, is defined by the nominal CRM cruise condition (Mach $= 0.85, C_L = 0.5$). Conditions 2 and 3, are defined as offsets of ± 0.025 in C_L relative to nominal cruise condition. Conditions 4 and 5 are defined as offsets of ± 0.01 in Mach number relative to the nominal condition, with the constraint that they maintain the same physical lift. The two buffet conditions are chosen to constrain buffet due to high lift and due to high Mach. The first buffet point is specified to be a 1.3 g margin on the highest lift at cruise (condition 3). The second buffet condition is placed at a high Mach design point ($M = 0.89$) with the constraint that the lift match that of the nominal cruise (condition 1). The three maneuver conditions consist of -1 g, and 2.5 g, maneuver conditions, and a 1 g cruise gust condition at which yield stress and buckling constraints are enforced.

The optimization problem is summarized in Table 2. The objective of the optimization is to minimize the average fuel burn at cruise. The fuel burn for each cruise condition is computed using the Breguet range equation,

$$\text{FB}_i = \text{LGW}\left(\exp\left(\frac{R\,\text{TSFC}}{V_i\,(L/D)_i}\right) - 1\right), \tag{15}$$

where LGW is the aircraft landing weight, R is the range, TSFC is the thrust-specific fuel consumption of the engine, and V_i and $(L/D)_i$ are the flight speed and lift-to-drag ratio at the

Number	Condition	FB Weight (T_i)	Mach	C_L/Lift	Altitude (ft)
1	Cruise	$1/5$	0.85	0.500	37 000
2	Cruise	$1/5$	0.85	0.475	37 000
3	Cruise	$1/5$	0.85	0.525	37 000
4	Cruise	$1/5$	0.84	0.512	37 000
5	Cruise	$1/5$	0.86	0.488	37 000
6	Buffet	0	0.85	0.683	37 000
7	Buffet	0	0.89	0.456	37 000
8	2.5 g Maneuver	0	0.64	$2.5 \cdot$ MTOW	0
9	-1 g Maneuver	0	0.64	$-$MTOW	0
10	1 g Maneuver	0	0.86	MTOW	27 300

Table 1: Flight conditions considered

i-th cruise condition, respectively. The landing weight of the aircraft is computed from the wingbox finite-element model along with the non-structural masses and fuselage.

A total of 1112 design variables are used for this design optimization. These design variables can be broken down into three groups: geometric variables, aerodynamic variables, and structural variables. These variables are listed in Table 2. The geometric design variables include the airfoil cross-sectional shape distribution over the span of the wing. The optimizer controls these shapes by perturbing the z-coordinate of each control points along the FFD surface containing the wing. The optimizer also controls the spanwise twist distribution of the wing by rigidly rotating set of chord-wise FFD control points.

The aerodynamic design variables include the angles of attack for each of the 10 flight conditions, used to matched the required lift at those conditions. In addition, we include the horizontal stabilizer incidence angles for each flight condition to make sure that the aircraft pitching moment is zero.

The remaining design variables consist of the structural design variables used to parameterize the wingbox. These include the stiffener pitch of the upper skin, lower skin, leading edge spar, and trailing edge spar, since the pitch is assumed to be constant across each of these components. As a result of the panel-based smeared stiffness approach, three additional design variables are added for each wingbox rib bay section: panel thickness, stiffener thickness, and stiffener height. Additionally, the panel length is included as a design variable for each panel to simplify panel buckling computations.

To achieve a meaningful and physically realizable design, at total of 1327 design constraints are enforced. We prevent buffet onset by using a separation-based constraint for two flight conditions, ensuring that all cruise points remain in the envelope defined by the 1.3 g margin to buffet onset, as required by flight regulations [57].

Several constraints are enforced to the geometry to prevent the optimizer from arriving at physically unrealizable designs. One of these is a volume constraint on the fuel bay of the wing that ensures that there is enough volume for the fuel required to complete the mission, including reserve fuel.

The remaining constraints are applied to the structure of the wing. The 2.5 g maneuver and 1 g

	Variable/function	Description	Quantity
minimize	$\sum_{i=1}^{N} T_i \text{FB}_i$	Average Fuel Burn	
with respect to	x_{α_i}	Angle of attack for each case	10
	x_{tail}	Tail trim angle for each case	10
	x_{twist}	Wing twist	8
	x_{airfoil}	FFD control points	240
	x_{thick}	Panel thickness skin/spars/ribs	287
	$x_{\text{stiff thick}}$	Panel stiffener thickness skin/spars/ribs	184
	$x_{\text{stiff height}}$	Panel stiffener height skin/spars/ribs	184
	$x_{\text{panel length}}$	Panel length skin/spars/ribs	184
	$x_{\text{stiff pitch}}$	Panel stiffener pitch skin/spars/ribs	4
	$C^*_{L_0}$	Nominal cruise target lift coefficient	1
		Total design variables	**1112**
subject to	$C_{L_i} = C^*_{L_i}$	Cruise and Buffet lift conditions	7
	$L = n_i W$	Maneuver lift conditions	3
	$c^i_{m_y} = 0$	Trimmed flight	10
	$t_{\text{LE}}/t_{\text{LE}_{\text{init}}} \geq 1.0$	Leading edge radius	20
	$t_{\text{TE}}/t_{\text{TE}_{\text{init}}} \geq 1.0$	Trailing edge thickness	20
	$(t/c)_{\text{TE,spar}} \geq 0.80(t/c)_{\text{TE spar}_{\text{init}}}$	Minimum trailing edge spar height	20
	$L_{\text{panel}} - x_{\text{panel length}} = 0$	Target panel length	266
	$\text{KS}_{\text{fail}} < 1.0$	2.5 g Material Failure	8
	$\text{KS}_{\text{buckling}} < 1.0$	2.5 g and -1 g Buckling	9
	$\left\lvert x_{\text{panel thick}_i} - x_{\text{panel thick}_{i+1}} \right\rvert \leq 0.0025$	Skin thickness adjacency	258
	$\left\lvert x_{\text{stiff thick}_i} - x_{\text{stiff thick}_{i+1}} \right\rvert \leq 0.0025$	Stiffener thickness adjacency	258
	$\left\lvert x_{\text{stiff height}_i} - x_{\text{stiff height}_{i+1}} \right\rvert$	Stiffener height adjacency	258
	$x_{\text{stiff thick}} - x_{\text{panel thick}} < 0.005$	Maximum stiffener-skin difference	172
	$\Delta z_{\text{TE,upper}} = -\Delta z_{\text{TE,lower}}$	Fixed trailing edge	8
	$\Delta z_{\text{LE,upper}} = -\Delta z_{\text{LE,lower}}$	Fixed leading edge	8
	$\text{Sep}_i \leq 0.04$	Buffet separation constraints	2
		Total constraints	**1327**

Table 2: Buffet-constrained aerostructural optimization problem used to define the uCRM-13.5 baseline.

cruise with gust conditions each use four KS material failure constraint aggregation functions: one each for the upper skin, lower skin, ribs, and spars. For these conditions, aggregated buckling constraints are enforced only for the upper skin, ribs, and spars. For the -1.0 g condition, only the buckling constraints are enforced for the lower skin, ribs, and spars. Finally, we apply hundreds linear adjacency constraints to ensure that the panel thickness, and stiffener thickness and heights do not change too much from panel to panel.

The result of this optimization problem is shown in Fig. 10, where the top view shows the C_p contours, the front view shows the shock, and the spanwise distributions show lift, twist, and thickness-to-chord ratio. We can see that the initial wing (left) exhibits a strong shock, which incurs a large fuel burn due to excessive wave drag. The optimized wing does away with most of the wave drag, and achieves a much better efficiency. The optimization is also able to reduce the wing thickness substantially, and produces a much more flexible wing, as seen from the front view of the wing deflection at the nominal cruise condition. This more flexible wing indicates that we might need to mitigate undesirable aeroelastic phenomena, such as aileron reversal and flutter.

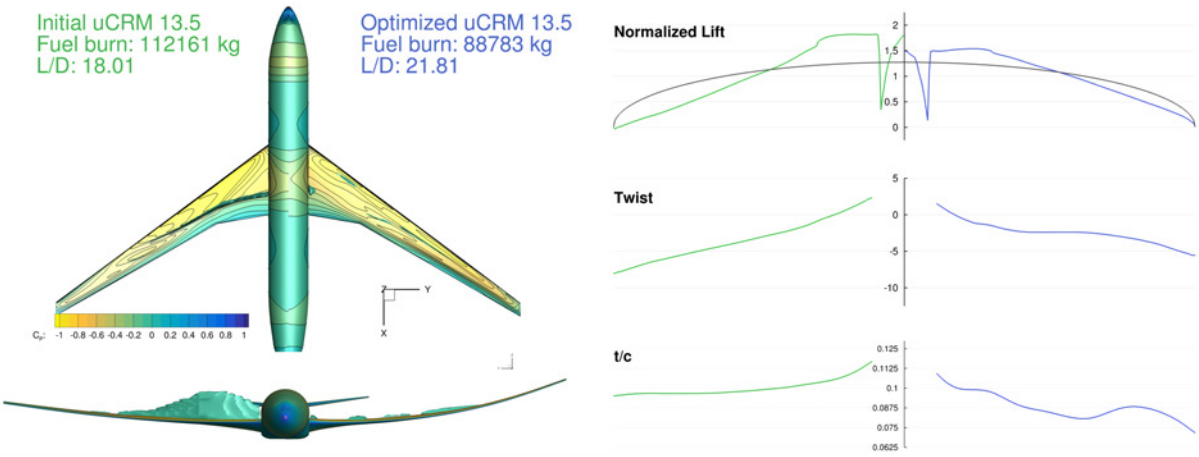

Figure 10: Comparison of initial uCRM-13.5 (left) with optimized uCRM-13.5 (right) aerostructural designs

4 OTHER APPLICATIONS

In addition to funding the development of the uCRM models, NASA also funded the investigation of two new airframe technologies—tow-steered composites and continuous morphing trailing edges—and a new aircraft configuration—the D8 double bubble.

4.1 Tow-steered composite wing

In the last 30 years since their introduction into aerospace applications, composites have become increasingly used, making up as much as 50% of modern aircraft by weight. With the introduction of automated fiber placement machines, the tow direction can now be steered spatially within each layer. The objective of this project was to exploit the use of tow-steered composites in the design of high aspect ratio wings.

Two aerostructural optimizations are performed for the uCRM-13.5 configuration: one with the full tow steering parametrization (the *steered* case), and one where the tow orientation is held fixed where the laminate thickness and other variables are still allowed to vary (the *unsteered* case). The optimization problem that we solve is very similar to the one solved for the uCRM-13.5 configuration, with the addition of the composite laminate design variables in the steered case, and the tow-steering variables in the steered case. The steered problem also includes tow curvature constraints due to manufacturing limitations. We provide more details on the problem formulation in a separate reference [31].

Fig. 11 compares the tow-steered and unsteered patterns for each ply. Due to the buckling constraints and the absence of stringers, the wing box panels are much thicker than in a realistic wing box. For both wings, the optimizer adds additional laminate thickness at the engine mounting location to deal with the local stress concentration. The main tow pattern for the upper and lower skin of the wing box both steer back towards the trailing edge at the root and the gradually sweep forward towards the tip. Overall, there is a 1% improvement in fuel burn for the tow-steered wing relative to the unsteered one.

4.2 Adaptive morphing trailing edge wing

Adaptive morphing trailing edge technology offers the potential to decrease the fuel burn of transonic transport aircraft by allowing wings to dynamically adjust to changing flight con-

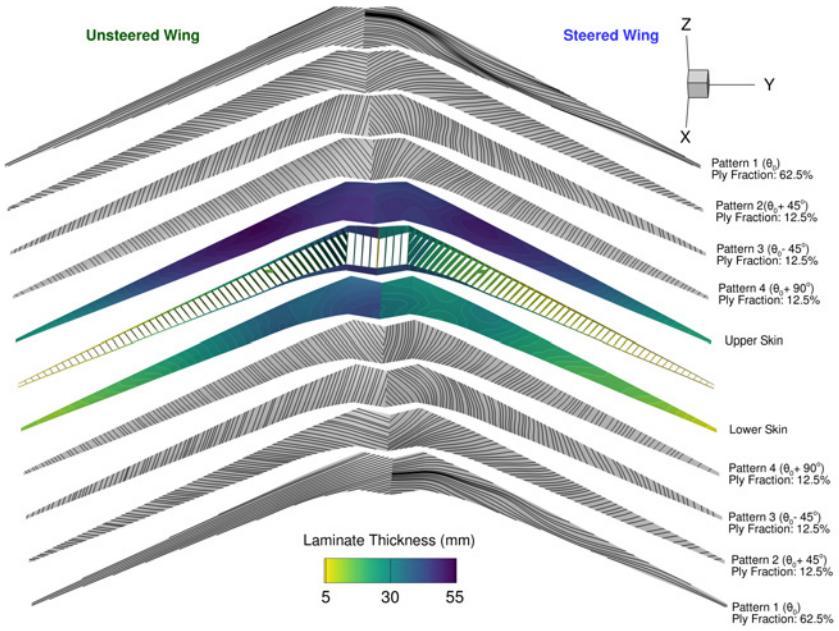

Figure 11: Comparison of optimal tow-steered versus unsteered aerostructural designs.

ditions [63, 64]. Current aircraft use flap and aileron droop to adjust the wing during flight. However, this approach offers only a limited number of degrees of freedom, and the gaps in the wing created when using these devices introduce unnecessary drag. Morphing trailing edges offers more degrees of freedom, with a seamless interface between the wing and control surfaces. Here, we seek to quantify the extent to which this technology can improve the fuel burn of transonic commercial transport sized aircraft. Starting from the uCRM geometry, we perform fixed-planform aerostructural optimizations of a clean sheet wing designed with the morphing trailing edge [32].

We consider an aerostructural optimization similar to the ones described above, but with added design variables that parametrize the trailing edge shape and can change for each flight condition. An optimization considering 7 flight conditions is shown in Fig. 12. The addition of morphing led to a substantial fuel burn reduction—over 5% in this case—largely through the reduction of structural weight. This reduction was enabled by the inboard shift of the maneuver load distribution resulting from the negative camber added to the outboard sections of the wing by the morphing. A more comprehensive set of optimization cases can be found in other work by the authors [32, 54, 65].

4.3 D8 transport aircraft

The D8 "double-bubble" is a new transport aircraft configuration proposed by Drela et al. [66, 67] that has the potential to provide large improvements in fuel efficiency. This aircraft configuration has been studied at the conceptual level and in low-speed wind tunnel tests, but there was, up to now, no higher fidelity transonic design. In this study, we use the conceptual design definition as a starting point and develop a high-fidelity aerostructural optimization problem for the D8 configuration using the MACH framework.

Here we summarize one of the results from our previous work [68]. Fig. 13 shows the results for the wing-body-tail optimizations of a D8 designed to fly at $M = 0.78$. The performance increase relative to the baseline design is significant: We achieve a fuel burn reduction of 27%.

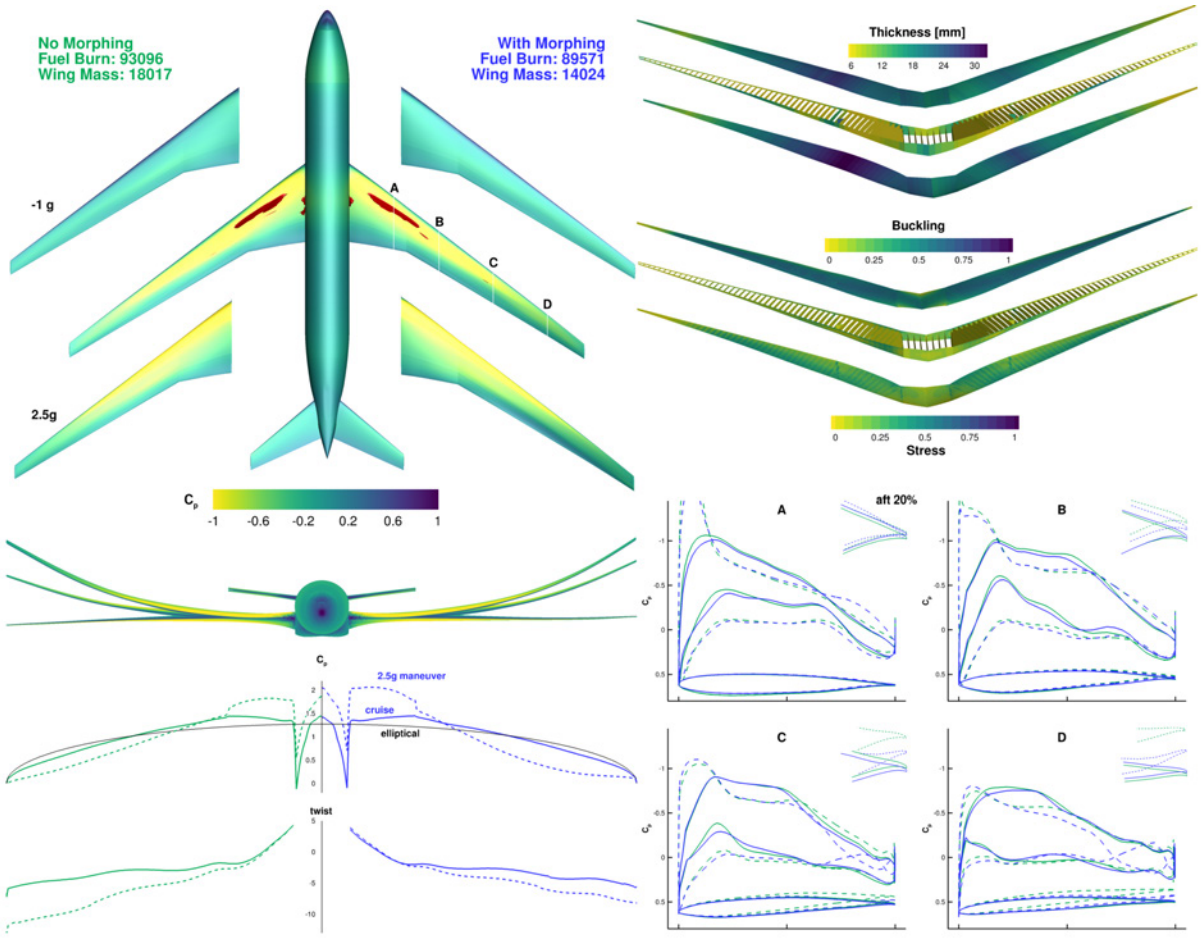

Figure 12: Adding morphing for 7 flight conditions reduced the fuel burn by 5.04%, and the structural weight by 25.8%.

There is a significant reduction in the wing t/c, as well as significant change in the airfoil shapes and sectional C_p. Most of the improvement in the design is aerodynamic: The L/D increased from 14.5 to 20, while the wing weight increased by 3%. This work confirms the viability of the D8 wing-body in the transonic regime and provides detailed transonic geometries for future work.

5 CONCLUSIONS

We presented a framework for high-fidelity aerodynamic and aerostructural design optimization of aircraft wings. The methods used in this framework successfully tackle the compounding challenges of modeling the wing with high fidelity, while optimizing it with respect to hundreds of design variables. The effectiveness of this framework leverages the use of high-performance parallel computing, fast solvers, state-of-the-art gradient-based optimization, and an efficient and accurate approach for computing the derivatives for the aerostructural solver via the coupled adjoint method.

We developed uCRM, a new open model for aeroelastic analysis and design studies, which includes both a wing with the same planform of the original CRM, and a wing with a high aspect ratio that is representative of the wings we expect to see in the next generation of long-range transport aircraft.

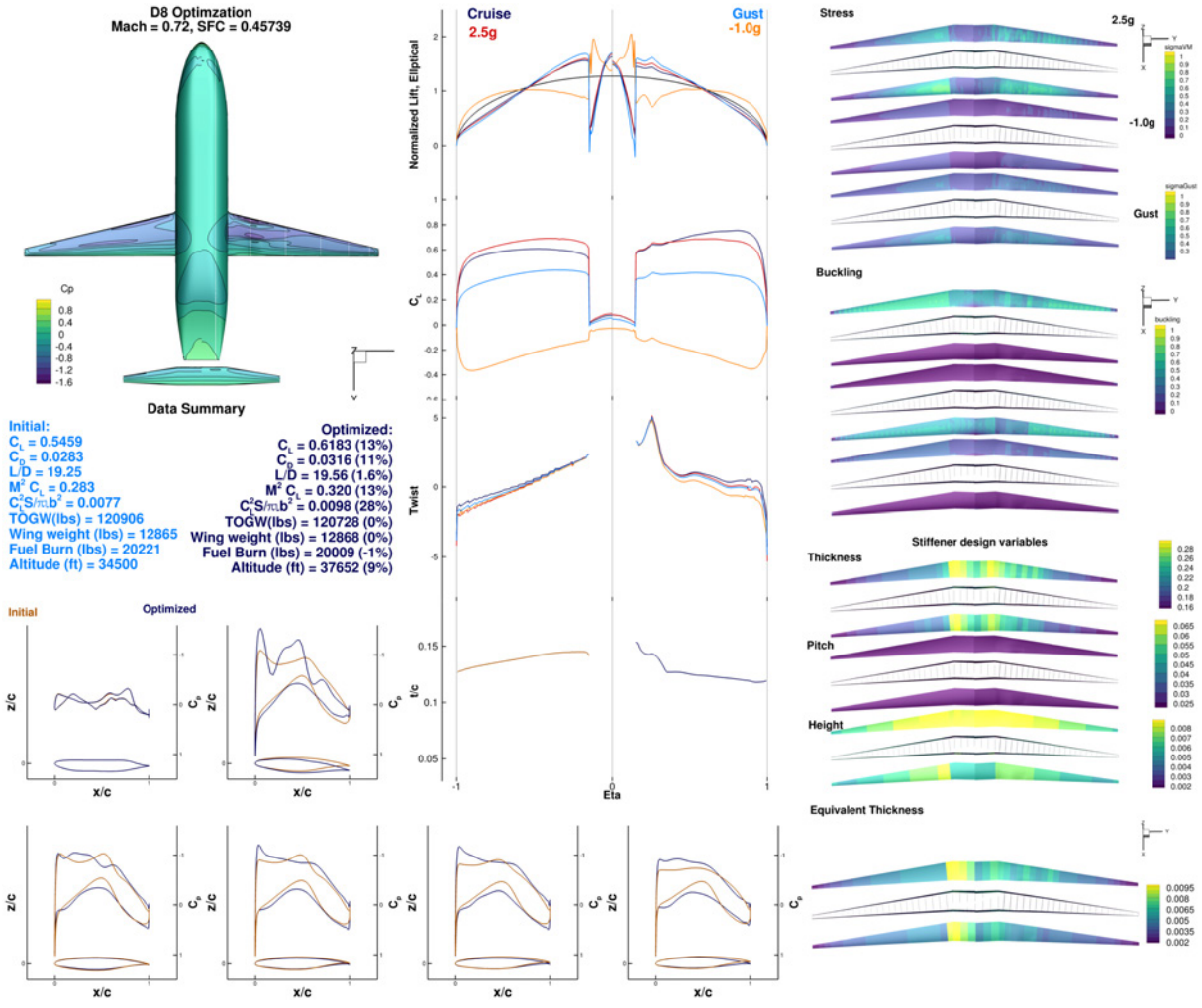

Figure 13: D8 optimization for $M = 0.78$.

We demonstrated the effectiveness of the framework by showing applications to the design of wings using two different airframe technologies, and to the design of the wings of an unconventional aircraft configuration.

ACKNOWLEDGMENTS

The authors would like to thank their collaborators at NASA, who supported this work through award number NNX11AI19A. This work used the Extreme Science and Engineering Discovery Environment (XSEDE), which is supported by National Science Foundation grant number ACI-1053575 [69].

6 REFERENCES

[1] Ashley, H. (1982). On making things the best — aeronautical uses of optimization. *Journal of Aircraft*, 19(1), 5–28.

[2] Green, J. A. (1987). Aeroelastic tailoring of aft-swept high-aspect-ratio composite wings. *Journal of Aircraft*, 24(11), 812–819. ISSN 0021-8669. doi:10.2514/3.45525.

[3] Grossman, B., Gurdal, Z., Strauch, G. J., et al. (1988). Integrated aerodynamic/structural design of a sailplane wing. *Journal of Aircraft*, 25(9), 855–860. doi:10.2514/3.45670.

[4] Grossman, B., Haftka, R. T., Kao, P.-J., et al. (1990). Integrated aerodynamic-structural design of a transport wing. *Journal of Aircraft*, 27(12), 1050–1056. doi:10.2514/3.45980.

[5] Jansen, P., Perez, R. E., and Martins, J. R. R. A. (2010). Aerostructural optimization of nonplanar lifting surfaces. *Journal of Aircraft*, 47(5), 1491–1503. doi:10.2514/1.44727.

[6] Kenway, G. K. W. and Martins, J. R. R. A. (2014). Multipoint high-fidelity aerostructural optimization of a transport aircraft configuration. *Journal of Aircraft*, 51(1), 144–160. doi:10.2514/1.C032150.

[7] Kroo, I. M., Altus, S., Braun, R. D., et al. (1994). Multidisciplinary optimization methods for aircraft preliminary design. In *5^{th} AIAA/USAF/NASA/ISSMO Symposium on Multidisciplinary Analysis and Optimization*. AIAA Paper 94-4325.

[8] Wakayama, S. (1998). *Multidisciplinary design optimization of the blended-wing-body*. American Institute of Aeronautics and Astronautics. doi:doi:10.2514/6.1998-4938.

[9] Martins, J. R. R. A. and Lambe, A. B. (2013). Multidisciplinary design optimization: A survey of architectures. *AIAA Journal*, 51(9), 2049–2075. doi:10.2514/1.J051895.

[10] Gill, P. E., Murray, W., and Saunders, M. A. (2002). SNOPT: An SQP algorithm for large-scale constrained optimization. *SIAM Journal of Optimization*, 12(4), 979–1006. doi:10.1137/S1052623499350013.

[11] Perez, R. E., Jansen, P. W., and Martins, J. R. R. A. (2012). pyOpt: A Python-based object-oriented framework for nonlinear constrained optimization. *Structural and Multidisciplinary Optimization*, 45(1), 101–118. doi:10.1007/s00158-011-0666-3.

[12] Martins, J. R. R. A. and Hwang, J. T. (2013). Review and unification of methods for computing derivatives of multidisciplinary computational models. *AIAA Journal*, 51(11), 2582–2599. doi:10.2514/1.J052184.

[13] Squire, W. and Trapp, G. (1998). Using complex variables to estimate derivatives of real functions. *SIAM Review*, 40(1), 110–112. ISSN 0036-1445 (print), 1095-7200 (electronic).

[14] Martins, J. R. R. A., Sturdza, P., and Alonso, J. J. (2003). The complex-step derivative approximation. *ACM Transactions on Mathematical Software*, 29(3), 245–262. doi:10.1145/838250.838251.

[15] Griewank, A. (2000). *Evaluating Derivatives*. Philadelphia: SIAM.

[16] Carle, A. and Fagan, M. (2000). ADIFOR 3.0 overview. Tech. Rep. CAAM-TR-00-02, Rice University.

[17] Giering, R. and Kaminski, T. (2002). Applying TAF to generate efficient derivative code of Fortran 77-95 programs. In *Proceedings of GAMM 2002, Augsburg, Germany*.

[18] Gockenbach, M. S. (2000). Understanding Code Generated by TAMC. IAAA Paper TR00-29, Department of Computational and Applied Mathematics, Rice University, Texas, USA.

[19] Hascoët, L. and Pascual, V. (2004). Tapenade 2.1 user's guide. Technical report 300, INRIA.

[20] Pascual, V. and Hascoët, L. (2005). Extension of TAPENADE towards Fortran 95. In H. M. Bücker, G. Corliss, P. Hovland, U. Naumann, and B. Norris (Eds.), *Automatic Differentiation: Applications, Theory, and Tools*, Lecture Notes in Computational Science and Engineering. Berlin, Germany: Springer.

[21] Mader, C. A., Martins, J. R. R. A., Alonso, J. J., et al. (2008). ADjoint: An approach for the rapid development of discrete adjoint solvers. *AIAA Journal*, 46(4), 863–873. doi:10.2514/1.29123.

[22] Lyu, Z., Kenway, G. K., Paige, C., et al. (2013). Automatic differentiation adjoint of the Reynolds-averaged Navier–Stokes equations with a turbulence model. In *21st AIAA Computational Fluid Dynamics Conference*. San Diego, CA. doi:10.2514/6.2013-2581.

[23] Peter, J. E. V. and Dwight, R. P. (2010). Numerical sensitivity analysis for aerodynamic optimization: A survey of approaches. *Computers and Fluids*, 39(3), 373–391. doi:10.1016/j.compfluid.2009.09.013.

[24] Mader, C. A. and Martins, J. R. R. A. (2013). Stability-constrained aerodynamic shape optimization of flying wings. *Journal of Aircraft*, 50(5), 1431–1449. doi:10.2514/1.C031956.

[25] Mader, C. A. and Martins, J. R. R. A. (2014). Computing stability derivatives and their gradients for aerodynamic shape optimization. *AIAA Journal*, 52(11), 2533–2546. doi:10.2514/1.J052922.

[26] Lyu, Z. and Martins, J. R. R. A. (2014). Aerodynamic design optimization studies of a blended-wing-body aircraft. *Journal of Aircraft*, 51(5), 1604–1617. doi:10.2514/1.C032491.

[27] Lyu, Z., Kenway, G. K. W., and Martins, J. R. R. A. (2015). Aerodynamic shape optimization investigations of the Common Research Model wing benchmark. *AIAA Journal*, 53(4), 968–985. doi:10.2514/1.J053318.

[28] Chen, S., Lyu, Z., Kenway, G. K. W., et al. (2016). Aerodynamic shape optimization of the Common Research Model wing-body-tail configuration. *Journal of Aircraft*, 53(1), 276–293. doi:10.2514/1.C033328.

[29] Kenway, G. K. W. and Martins, J. R. R. A. (2015). Multipoint aerodynamic shape optimization investigations of the Common Research Model wing. In *Proceedings of the AIAA Science and Technology Forum and Exposition (SciTech)*. Kissimmee, FL. doi:10.2514/6.2015-0264.

[30] Liem, R. P., Kenway, G. K. W., and Martins, J. R. R. A. (2015). Multimission aircraft fuel burn minimization via multipoint aerostructural optimization. *AIAA Journal*, 53(1), 104–122. doi:10.2514/1.J052940.

[31] Brooks, T. R., Kennedy, G. J., and Martins, J. R. R. A. (2017). High-fidelity multipoint aerostructural optimization of a high aspect ratio tow-steered composite wing. In *Proceedings of the 58th AIAA/ASCE/AHS/ASC Structures, Structural Dynamics, and Materials Conference, AIAA SciTech Forum*. Grapevine, TX. doi:10.2514/6.2017-1350.

[32] Burdette, D. A., Kenway, G. K., and Martins, J. R. R. A. (2016). Performance evaluation of a morphing trailing edge using multipoint aerostructural design optimization. In *57th AIAA/ASCE/AHS/ASC Structures, Structural Dynamics, and Materials Conference*. American Institute of Aeronautics and Astronautics. doi:10.2514/6.2016-0159.

[33] Kenway, G. W. K. and Martins, J. R. R. A. (2015). High-fidelity aerostructural optimization considering buffet onset. In *Proceedings of the 16th AIAA/ISSMO Multidisciplinary Analysis and Optimization Conference*. Dallas, TX. AIAA 2015-2790.

[34] Kenway, G. K. W., Kennedy, G. J., and Martins, J. R. R. A. (2014). Aerostructural optimization of the Common Research Model configuration. In *15th AIAA/ISSMO Multidisciplinary Analysis and Optimization Conference*. Atlanta, GA. doi:10.2514/6.2014-3274. AIAA 2014-3274.

[35] van der Weide, E., Kalitzin, G., Schluter, J., et al. (2006). Unsteady turbomachinery computations using massively parallel platforms. In *Proceedings of the 44th AIAA Aerospace Sciences Meeting and Exhibit*. Reno, NV. AIAA 2006-0421.

[36] Sederberg, T. W. and Parry, S. R. (1986). Free-form deformation of solid geometric models. *SIGGRAPH Comput. Graph.*, 20(4), 151–160. ISSN 0097-8930. doi:10.1145/15886.15903.

[37] Kenway, G. K., Kennedy, G. J., and Martins, J. R. R. A. (2010). A CAD-free approach to high-fidelity aerostructural optimization. In *Proceedings of the 13th AIAA/ISSMO Multidisciplinary Analysis Optimization Conference*. Fort Worth, TX. doi:10.2514/6.2010-9231. AIAA 2010-9231.

[38] Kenway, G. K. W., Kennedy, G. J., and Martins, J. R. R. A. (2014). Scalable parallel approach for high-fidelity steady-state aeroelastic analysis and derivative computations. *AIAA Journal*, 52(5), 935–951. doi:10.2514/1.J052255.

[39] Luke, E., Collins, E., and Blades, E. (2012). A fast mesh deformation method using explicit interpolation. *Journal of Computational Physics*, 231(2), 586–601. ISSN 0021-9991. doi:10.1016/j.jcp.2011.09.021.

[40] Kennedy, G. J. and Martins, J. R. R. A. (2014). A parallel finite-element framework for large-scale gradient-based design optimization of high-performance structures. *Finite Elements in Analysis and Design*, 87, 56–73. doi:10.1016/j.finel.2014.04.011.

[41] Brown, S. A. (1997). Displacement extrapolation for CFD+CSM aeroelastic analysis. In *Proceedings of the 35th AIAA Aerospace Sciences Meeting*. Reno, NV. AIAA 1997-1090.

[42] Martins, J. R. R. A., Kenway, G. K. W., and Brooks, T. R. (2016). Multidisciplinary design optimization of aircraft configurations—part 2: High-fidelity aerostructural optimization. Lecture series, Von Karman Institute for Fluid Dynamics, Rode Saint Genèse, Belgium. ISSN0377-8312.

[43] Martins, J. R. R. A., Alonso, J. J., and Reuther, J. J. (2005). A coupled-adjoint sensitivity analysis method for high-fidelity aero-structural design. *Optimization and Engineering*, 6(1), 33–62. doi:10.1023/B:OPTE.0000048536.47956.62.

[44] Maute, K., Nikbay, M., and Farhat, C. (2001). Coupled analytical sensitivity analysis and optimization of three-dimensional nonlinear aeroelastic systems. *AIAA Journal*, 39(11), 2051–2061.

[45] Irons, B. M. and Tuck, R. C. (1969). A version of the aitken accelerator for computer iteration. *International Journal for Numerical Methods in Engineering*, 1(3), 275–277.

[46] Martins, J. R. R. A., Alonso, J. J., and Reuther, J. J. (2004). High-fidelity aerostructural design optimization of a supersonic business jet. *Journal of Aircraft*, 41(3), 523–530. doi:10.2514/1.11478.

[47] Vassberg, J. C., DeHaan, M. A., Rivers, S. M., et al. (2008). Development of a common research model for applied CFD validation studies. AIAA 2008-6919.

[48] Lyu, Z., Kenway, G. K. W., and Martins, J. R. R. A. (2014). RANS-based aerodynamic shape optimization investigations of the common research model wing. In *Proceedings of the AIAA Science and Technology Forum and Exposition (SciTech)*. National Harbor, MD. doi:10.2514/6.2014-0567. AIAA 2014-0567.

[49] Kenway, G. K. W. and Martins, J. R. R. A. (2016). Multipoint aerodynamic shape optimization investigations of the Common Research Model wing. *AIAA Journal*, 54(1), 113–128. doi:10.2514/1.J054154.

[50] LeDoux, S. T., Vassberg, J. C., Young, D. P., et al. (2015). Study based on the AIAA aerodynamic design optimization discussion group test cases. *AIAA Journal*. doi:10.2514/1.j053535.

[51] LeDoux, S. T., Young, D. P., Fugal, S., et al. (2015). A study based on the AIAA aerodynamic design optimization discussion group test cases. In *53rd AIAA Aerospace Sciences Meeting*. American Institute of Aeronautics and Astronautics (AIAA). doi:10.2514/6.2015-1717.

[52] Vassberg, J. and Jameson, A. (2014). Influence of shape parameterization on aerodynamic shape optimization. Tech. rep., Von Karman Institute, Brussels, Belgium.

[53] Carrier, G., Destarac, D., Dumont, A., et al. (2014). Gradient-based aerodynamic optimization with the elsA software. In *52nd Aerospace Sciences Meeting*. doi:10.2514/6.2014-0568.

[54] Burdette, D., Kenway, G. K. W., Lyu, Z., et al. (2015). Aerostructural design optimization of an adaptive morphing trailing edge wing. In *Proceedings of the AIAA Science and Technology Forum and Exposition (SciTech)*. Kissimmee, FL. doi:10.2514/6.2016-1294.

[55] Brooks, T. R., Kennedy, G. J., and Martins, J. R. R. A. (2016). High-fidelity aerostructural optimization of a high aspect ratio tow-steered wing. In *57th AIAA/ASCE/AHS/ASC Structures, Structural Dynamics, and Materials Conference*. American Institute of Aeronautics and Astronautics. doi:10.2514/6.2016-1179.

[56] Chin, T. W. and Kennedy, G. (2016). Large-scale compliance-minimization and buckling topology optimization of the undeformed common research model wing. In *57th AIAA/ASCE/AHS/ASC Structures, Structural Dynamics, and Materials Conference*. American Institute of Aeronautics and Astronautics. doi:10.2514/6.2016-0939.

[57] Kenway, G. K. W. and Martins, J. R. R. A. (2017). Buffet onset constraint formulation for aerodynamic shape optimization. *AIAA Journal*. doi:10.2514/1.J055172. (In press).

[58] Vassberg, J. (2011). A unified baseline grid about the Common Research Model wing/body for the Fifth AIAA CFD Drag Prediction Workshop (invited). In *29th AIAA Applied Aerodynamics Conference*. doi:10.2514/6.2011-3508.

[59] Anonymous (1998). 777-200/300 airplane characteristics for airport planning. Tech. Rep. D6-58329, Boeing Commercial Airplanes.

[60] Kennedy, G. J., Kenway, G. K. W., and Martins, J. R. R. A. (2014). High aspect ratio wing design: Optimal aerostructural tradeoffs for the next generation of materials. In *Proceedings of the AIAA Science and Technology Forum and Exposition (SciTech)*. National Harbor, MD. doi:10.2514/6.2014-0596.

[61] Akgün, M. A., Haftka, R. T., Wu, K. C., et al. (2001). Efficient structural optimization for multiple load cases using adjoint sensitivities. *AIAA Journal*, 39(3), 511–516.

[62] Poon, N. M. K. and Martins, J. R. R. A. (2007). An adaptive approach to constraint aggregation using adjoint sensitivity analysis. *Structural and Multidisciplinary Optimization*, 34(1), 61–73. doi:10.1007/s00158-006-0061-7.

[63] Martins, J. R. R. A. (2016). *Encyclopedia of Aerospace Engineering*, vol. Green Aviation, chap. Fuel burn reduction through wing morphing. Wiley. ISBN 978-1-118-86635-1, pp. 75–79. doi:10.1002/9780470686652.eae1007.

[64] Kota, S., Osborn, R., Ervin, G., et al. (2007). Mission adaptive compliant wing—design, fabrication and flight test. Tech. Rep. RTO-MP-AVT-168, NATO Research and Technology Organization.

[65] Burdette, D. A., Kenway, G. K. W., and Martins, J. R. R. A. (2016). Aerostructural design optimization of a continuous morphing trailing edge aircraft for improved mission performance. In *17th AIAA/ISSMO Multidisciplinary Analysis and Optimization Conference*. doi:10.2514/6.2016-3209.

[66] Drela, M. (2011). Development of the D8 transport configuration. In *29th AIAA Applied Aerodynamics Conference*. American Institute of Aeronautics and Astronautics. doi:10.2514/6.2011-3970.

[67] Uranga, A., Drela, M., Greitzer, E., et al. (2014). Preliminary experimental assessment of the boundary layer ingestion benefit for the d8 aircraft. In *52nd Aerospace Sciences Meeting*. American Institute of Aeronautics and Astronautics (AIAA). doi:10.2514/6.2014-0906.

[68] Mader, C. A., Kenway, G. K., Martins, J., et al. (2017). Aerostructural optimization of the d8 wing with varying cruise mach numbers. In *18th AIAA/ISSMO Multidisciplinary Analysis and Optimization Conference*. American Institute of Aeronautics and Astronautics. doi:10.2514/6.2017-4436.

[69] Towns, J., Cockerill, T., Dahan, M., et al. (2014). XSEDE: Accelerating scientific discovery. *Computing in Science & Engineering*, 16(5), 62–74. doi:10.1109/MCSE.2014.80.

COPYRIGHT STATEMENT